

# Phase retrieval beyond the homogeneous object assumption for X-ray in-line holographic imaging

JENS LUCHT,<sup>1,2,\*</sup> LEON M. LOHSE,<sup>1,2,3</sup> THORSTEN HOHAGE,<sup>4</sup> AND TIM SALDITT<sup>1,2</sup>

<sup>1</sup>Georg-August-Universität Göttingen, Institut für Röntgenphysik, Friedrich-Hund-Platz 1, D-37077 Göttingen, Germany

<sup>2</sup>Max Planck School of Photonics, Albert-Einstein-Straße 15, D-07745 Jena, Germany

<sup>3</sup>Deutsches Elektronen-Synchrotron DESY, Notkestraße 85, D-22607 Hamburg, Germany

<sup>4</sup>Georg-August-Universität, Institut für Numerische und Angewandte Mathematik Göttingen, Lotzestraße 16-18, D-37083 Göttingen, Germany

\*jens.lucht@uni-goettingen.de

**Abstract:** X-ray near field holography has proven to be a powerful 2D and 3D imaging technique with applications ranging from biomedical research to material sciences. To reconstruct meaningful and quantitative images from the measurement intensities, however, it relies on computational phase retrieval which in many cases assumes the phase-shift and attenuation coefficient of the sample to be proportional. Here, we demonstrate an efficient phase retrieval algorithm that does not rely on this homogeneous-object assumption and is a generalization of the well-established contrast-transfer-function (CTF) approach. We then investigate its stability and present an experimental study comparing the proposed algorithm with established methods. The algorithm shows superior reconstruction quality compared to the established CTF-based method at similar computational cost. Our analysis provides a deeper fundamental understanding of the homogeneous object assumption and the proposed algorithm will help improve the image quality for near-field holography in biomedical applications.

## 1. Introduction

X-ray phase contrast imaging tomography (XPCT) enables three-dimensional (3D) imaging at scalable field of view and resolution for a wide range of applications from biomedical research to material sciences [1, 2]. Due to the penetration power of hard X-rays, XPCT is compatible with bulk specimen, complex sample environments, and in operando configurations. For samples which lack sufficient absorption such as soft unstained tissues, or more generally soft matter, phase contrast based on free propagation and self-interference has significantly extended the applicability and use of computed tomography (CT). Compared to other variants of X-ray phase contrast imaging (XPCI) such as grating-based, speckle-based, or ptychographic approaches, propagation based imaging (PBI) is particularly attractive, due to the lack of additional optical elements, and the fact that no lateral scanning of the sample is required. Combined with synchrotron radiation of high spatial coherence, resolution in the sub-micrometer regime is routinely available, and even sub-100 nm can be achieved when using divergent beams and geometric magnification [3, 4]. For two-dimensional (2D) imaging (XPCI), full field imaging with sub-15 nm has been recently demonstrated [5].

A crucial step for XPCI and XPCT is the phase retrieval step, where the task is to recover the phase from the intensity-only measurements, see for example [6]. In PBI, the signal is given by near field diffraction patterns or inline *holograms*, formed by self interference downstream from the sample as governed by the Fresnel number  $f$ . These interference patterns are the input of the phase retrieval and reflect the local phase shifts which the object has imparted upstream on the beam. Note, that parallel beam or cone beam illuminations are equally possible and equivalent up to geometric magnification and an effective rescaling of the propagation distance, as expressed by the Fresnel scaling theorem [7]. In fact, in the experimental part of this work, we rely on a

waveguide, acting as quasi point source and generating an aberration free divergent wavefront for magnification.

Phase retrieval for PBI is actively researched and numerous algorithms have been developed so far. Examples are transport-of-intensity (TIE) based approaches [8, 9], which are restricted to large  $f$  and are often for data acquired at laboratory X-ray sources, iterative projection type algorithms like Gerchberg-Saxton and its derivatives [10–12], as well as gradient decent-type algorithms [13–15]. In particular for CT, where easily up a few thousands of projections are acquired, computational efficiency is very important, and the vast majority of XPCT data is phased by direct but approximative methods, notably in the TIE regime by Paganin’s method [8], and in at small  $f$  by the contrast transfer function (CTF) approach [16]. Hence, phase retrieval is mostly performed by regularized Fourier filtering. This is fast for sure, but is it also sufficiently exact and general enough for the wide range of applications? In the derivations of the most common phase retrieval schemes, the assumption of optically weak and/or homogeneous objects is ubiquitous and presumingly overly restrictive. Strictly speaking, this results in an inexact model and inconsistency with the acquired data. It may be expected, that these inconsistencies cause artifacts in reconstructions, which degrade reconstruction quality. In the present work, we generalize CTF-based phase retrieval to independent (uncoupled) reconstruction of phase and amplitude, with quantified stability analysis, and present a detailed analysis of the homogeneity assumption within the CTF-framework. We study the consequences of posing or relaxing the assumptions for different parameter settings based on numerical simulations and experimental data acquired for a non-homogeneous test object.

Closely related to the presented approach is [17], where the authors compare frequency-dependent Tikhonov and total variation (TV) regularization within the CTF approximation. In contrast to our approach constraints on the object, such as (non-)negativity or compact support, cannot be imposed on the solution. Moreover, a different iteration scheme is used. In [18] the CTF is combined with Alternating Direction Method of Multipliers (ADMM), but under the assumption of pure-phase or single material objects and the use of sparsity-promoting regularization. Possibly, [19] is the closest related work to the present one, where the authors present a CTF-based single-distance reconstruction without homogeneity assumption but with a TV-prior. However, in the present work, we focus on a comparison and analysis of the homogeneity assumption within the CTF-framework while not relying on TV priors.

The manuscript is organized as follows: After this introduction, section 2 presents the basic theory, starting with the conventional CTF which we rephrase for notational clarity before giving the generalisation for the non-homogeneous case. In section 3, the results of the stability analysis are given for the relevant experimental parameters, and the corresponding regularization strategy as a function of the given number of different defocus distances. Finally, state-of-the-art nanoscale XPCI experiments are shown in section 4, and are used to test and illustrate the capability of the present phase retrieval approach.

## 2. Fresnel near-field holography

Let  $F$  be our Fresnel imaging (forward) operator given by

$$I \approx F(f) \equiv |\mathcal{D}(\exp(f))|^2 \quad (1)$$

with  $I$  the measured (noisy) intensities  $I$ , the object to reconstruct  $f = \mu + i\phi$  under the projection approximation, given by a phase shift  $\phi \leq 0$  and absorption  $\mu \leq 0$ , and the Fresnel propagator  $\mathcal{D}$  for any suitable function  $\psi$  given by [20]

$$\mathcal{D}(\psi) \equiv \mathcal{F}^{-1}(m_f(\xi) \cdot \mathcal{F}(\psi)(\xi)), \quad (2)$$

with transfer function  $m_f(\xi) = \exp\left(-\frac{i|\xi|^2}{4\pi f}\right)$ , two-dimensional Fourier transform  $\mathcal{F}$ , respectively its inverse  $\mathcal{F}^{-1}$ , and spatial frequency  $\xi$ . We call the intensity images *holograms* due to their in-

line holographic origin. We see,  $F$  clearly is a nonlinear operator due to the complex exponential and squared modulus. Experimental parameters can be condensed into a dimensionless quantity known as Fresnel number, given by  $\mathfrak{f} = \frac{s^2}{\lambda z_{12}}$ , with photon wavelength  $\lambda$ , free-space propagation distance  $z_{12}$  between object and detector, and reference scale  $s$ . We set this scale to the pixel size of the imaging system  $\Delta_x$  and will use the term Fresnel number for this *pixel Fresnel number*.

In projection approximation the relation between the energy  $E$  and 3D-spatially  $(x, y, z)$  dependent (complex) refractive index  $n(E; x, y, z) = 1 - \delta(E; x, y, z) + i\beta(E; x, y, z)$  and measured *2D-projection images* is given by,  $\phi(E; x, y) = -k \int \delta(E; x, y, z) dz$  and  $\mu(E; x, y) = -k \int \beta(E; x, y, z) dz$ , respectively, where the optical axis in parallel beam geometry is chosen as  $z$ -axis, and  $k = 2\pi/\lambda$  is the wave number in vacuum. Henceforward, we assume a constant energy  $E$  and do not state its dependence explicitly. Note that in our definition phase delay and absorption are non-positive.

An object is called *optically weak* if  $|\phi|, |\mu| \ll 1$ . For such objects the Fresnel imaging operator (1) can be approximated by the well-known *contrast transfer function* (CTF). Mathematically, the CTF corresponds to linearization of (1) with respect to the object  $f$ . The linearized CTF forward operator is given by  $L(f)$ , where

$$I \approx L(f) \equiv 1 + 2\Re[\mathcal{D}(f)], \quad (3)$$

with real-part operator  $\Re$ . More commonly,  $L$  is expressed in Fourier space for phase  $\phi$  and absorption  $\mu$ ,

$$L(f) = 1 + 2\mathcal{F}^{-1} \left( s_{\mathfrak{f}}(\xi) \cdot \mathcal{F}(\phi)(\xi) + c_{\mathfrak{f}}(\xi) \cdot \mathcal{F}(\mu)(\xi) \right), \quad (4)$$

with  $s_{\mathfrak{f}}(\xi) \equiv \sin\left(\frac{|\xi|^2}{4\pi\mathfrak{f}}\right)$  and  $c_{\mathfrak{f}}(\xi) \equiv \cos\left(\frac{|\xi|^2}{4\pi\mathfrak{f}}\right)$

the corresponding transfer functions. For a review on the validity conditions of the CTF approximation we refer to [21].

### 2.1. CTF-based phase retrieval

The task of phase retrieval is to reconstruct the unknown object  $f$  from a set of intensity-only holograms  $I_j$ , where  $j = 1, \dots, J$ , are holograms at different Fresnel numbers  $\mathfrak{f}_j$ , e. g. by variation of the defocus distance. Using the linear CTF operator poses are linear inverse problem. We express multiple holograms  $I_j$  by using the linearity of the CTF in a matrix formalism that we adapt from [17].

If we write the holograms as a stacked vector  $I$ , define the transfer matrix  $M$ , and (with a slight abuse of notation, identifying  $\mathbb{C}$  with  $\mathbb{R}^2$ ) express the complex-valued object as vector  $(i\phi + \mu) \simeq (\phi, \mu)^\top$ , then

$$I = \begin{pmatrix} I_1 \\ \vdots \\ I_J \end{pmatrix}, \quad M = 2 \begin{pmatrix} s_1 & c_1 \\ \vdots & \vdots \\ s_J & c_J \end{pmatrix}, \quad f = \begin{pmatrix} \phi \\ \mu \end{pmatrix}, \quad (5)$$

where  $s_j = s_{\mathfrak{f}_j}$ ,  $c_j = c_{\mathfrak{f}_j}$  denote the corresponding transfer functions defined in (4) at Fresnel number  $\mathfrak{f}_j$ . The matrix CTF operator is thus given by,

$$I \simeq L(f) = 1 + \mathcal{F}^{-1} M \mathcal{F}(f), \quad (6)$$

where the Fourier transforms  $\mathcal{F}$ ,  $\mathcal{F}^{-1}$  and scalar multiplication by two are meant element-wise. Note that we use the diagonality of the Fresnel propagator in Fourier space and thus  $M$  is expressed *per frequency*.

Phase retrieval amounts to the solution of the regularized linear inverse problem,

$$f_{\dagger} = \arg \min_f \left\{ \|L(f) - I\|^2 + \|A\mathcal{F}f\|^2 \right\}, \quad (7)$$

where  $A = A(\xi) = \text{diag} \left( 2\sqrt{\alpha_{\phi}(\xi)}, 2\sqrt{\alpha_{\mu}(\xi)} \right)$  denotes a frequency-weighted Tikhonov-type regularization operator, with  $\alpha_{\phi}, \alpha_{\mu} \geq 0$ .

The solution of least-squares problem in (7) for  $\alpha_{\phi}, \alpha_{\mu} > 0$  is given in closed-form by,

$$f_{\dagger} = \left( L^*L + \mathcal{F}^{-1}A^*A\mathcal{F} \right)^{-1} (L^*I) = \mathcal{F}^{-1} \left[ (M^*M + A^*A)^{-1} (M^*\mathcal{F}(I - 1)) \right], \quad (8)$$

where the superscript \* denotes the adjoint. Here we used, that the Fourier transform is unitary,  $\mathcal{F}^* = \mathcal{F}^{-1}$ . Explicitly, the solution in Fourier space is,

$$\begin{pmatrix} \mathcal{F}\phi_{\dagger} \\ \mathcal{F}\mu_{\dagger} \end{pmatrix} = \frac{8}{D} \begin{pmatrix} \alpha_{\mu} + \sum_j c_j^2 & -\sum_j c_j s_j \\ -\sum_j c_j s_j & \alpha_{\phi} + \sum_j s_j^2 \end{pmatrix} \begin{pmatrix} \sum_j s_j (\mathcal{F}I_j - 1) \\ \sum_j c_j (\mathcal{F}I_j - 1) \end{pmatrix}, \quad (9)$$

where  $D = \det(M^*M + A^*A)$  (see appendix A). For readability we have omitted the summation limits which are  $j = 1$  to  $j = J$ . Written in components, this coincides with the formula presented in [22]. We remark that due to (9) phase retrieval without further a-priori information is only uniquely feasible for *at least two holograms*, i.e.,  $J \geq 2$ . This goes along with the intuition that a meaningful estimation of two unknowns ( $\phi$  and  $\mu$ ) from a single data point is not uniquely possible *without additional assumptions on the the solution*. As shown in [23, 24], the assumption of compactness of the support of  $\phi$  and  $\mu$  suffices to restore uniqueness and even stability.

### 2.1.1. Homogeneous objects

One ubiquitous assumption in XPCI is that the sample solely composed by a single material, what we refer to as *homogeneous* or *single material object* (SMO) [8]. This implies, that phase and absorption images are proportional by  $\frac{\mu}{\phi} = \frac{\beta}{\delta} = \gamma = \text{const}$ , where  $\delta$  and  $\beta$  are defined after (2). Thus, the number of unknowns effectively reduces from two to one, i. e.  $f = (i + \gamma)\phi$ , but introduces an additional parameter  $\gamma$  that have to be determined *a priori*.

Inserting the homogeneous object assumption into the CTF model, we get [16, 25]

$$H_{\gamma}(\phi) = 1 + \mathcal{F}^{-1}M_{\gamma}\mathcal{F}\phi, \quad \text{with} \quad M_{\gamma} = 2 \begin{pmatrix} s_1 + \gamma c_1 \\ \vdots \\ s_J + \gamma c_J \end{pmatrix}. \quad (10)$$

Note that  $M_{\gamma}$  is a  $(J \times 1)$  matrix and the unknown variable is  $\phi$ . By the reduction of the unknowns from two to one, also reconstructions from single-exposures are possible, but technically only for homogeneous objects with known and well-defined  $\gamma$ .

Contrary to this, many samples are composed of different materials with significantly different refractive indices. We call this kind of objects *inhomogeneous* or *multi-material objects*. A prominent example is contrast-enhancing staining. For inhomogeneous samples, the homogeneous object assumption is an inexact model. A unique choice of  $\gamma$  for such samples is not possible.

### 2.1.2. Constrained CTF

Standard CTF-based phase retrieval in form of Fourier filters does not allow to impose prior knowledge of the sample on the reconstruction. Object constraints, such as a spatial support,

(non-)negativity or box-constraints. Recently, we reported on a framework, which allows to incorporate such constraints to CTF phase retrieval with homogeneity assumption [15].

Mathematically, such object priors restrict the space of possible solutions to a proper closed, convex subset  $C$ , *i. e.* we require  $f_{\dagger} \in C \subseteq L^2(\mathbb{R}^2)$ . Thus, constrained CTF phase retrieval corresponds to the minimization of

$$f_{\dagger} = \arg \min_{f \in C} \left\{ \|L(f) - I\|^2 + \|A\mathcal{F}f\|^2 \right\}. \quad (11)$$

For (11) no closed-form or single step solution exists. However, a solution can be computed iteratively with the Alternating Direction Method of Multipliers (ADMM) [26, 27]. The iteration update for CTF-ADMM is given by,

$$\begin{aligned} f_{k+1} &= \arg \min_{f \in L^2(\mathbb{R}^2)} \left\{ \|L(f) - I\|^2 + \|A\mathcal{F}f\|^2 + \tau \|f - (g_k - h_k)\|^2 \right\} \\ &= \left( L^*L + \mathcal{F}^{-1}A^*A\mathcal{F} + \tau \mathbb{I} \right)^{-1} (L^*I + \tau(g_k - h_k)) \end{aligned} \quad (12a)$$

$$g_{k+1} = \Pi_C(f_{k+1} + h_k) \quad (12b)$$

$$h_{k+1} = h_k + f_{k+1} - g_{k+1}, \quad (12c)$$

where  $\mathbb{I}$  is the identity matrix,  $g, h$  are auxiliary variables initialized with  $g_0, h_0 = 0$ ,  $\tau > 0$  is a proximity parameter and  $\Pi_C(f) := \operatorname{argmin}_{h \in C} \|f - h\|$  is the metric projection onto  $C$ . In (12) we see the splitting into the so-called proximal mapping [28, 29] of the CTF inversion (12a) and object constraints (12b). Note that both solutions are given in closed form and no sub-iterations are needed. We apply a Nesterov-type accelerated ADMM variant; for its details we refer to [30].

To summarize, we now have four possible combinations of CTF phase retrieval variants, *i. e.*

1. with homogeneous object assumption, without object constraints (HomCTF),
2. with homogeneous object assumption, with object constraints (HomCTF  $\phi \in C$ ),
3. without homogeneous object assumption, without object constraints (CTF),
4. without homogeneous object assumption, with object constraints (CTF  $f \in C$ ).

### 3. Stability analysis

In this section we analyze the influence of the homogeneity assumption on the stability of the phase retrieval and consequences for phase retrieval without it. To do so, we compare the singular values of the corresponding transfer matrices, which can be interpreted as effective contrast transfer or signal per frequency. The higher the singular value, the higher the effective signal and thus the more robust is the phase retrieval against noise. Vice versa, near-zero or zero singular values correspond to vanishing effective signal, and near singular matrices, whose inversion for phase retrieval could be heavily distorted by noise.

We note that the singular values of the not regularized and unconstrained forward operator are overly pessimistic stability predictions. The use of additional a-priori assumption such as object constraints, e.g. compact spatial support or (non-)negativity, has strong influence [24]. Nevertheless, the singular values give an access to the general behavior of the (linearized) system and could be used to optimize experimental parameter, for example an optimal set of Fresnel numbers as reported for the homogeneous CTF in [22].

Here we use the normalized transfer matrix  $\tilde{M}$ , where we omit the multiplication by two as defined in (5); likewise, for the homogeneous transfer matrix  $\tilde{M}_\gamma$ . Thus, direct computation of the (smallest) singular value  $\sigma_-$ , of the  $\tilde{M}$ , yields,

$$\sigma_-^2(\tilde{M})(\xi) = \frac{J}{2} - \frac{1}{2} \left( J^2 - 4 \sum_{k=1}^J \sum_{j=k+1}^J \sin^2 \chi_{kj}(\xi) \right)^{\frac{1}{2}}, \quad (13)$$

where we used the difference phase chirp  $\chi_{kj}$ , given by  $\chi_{jk}(\xi) \equiv \frac{|\xi|^2}{4\pi} \left( \frac{1}{\tilde{f}_k} - \frac{1}{\tilde{f}_j} \right) \equiv \frac{|\xi|^2}{4\pi\tilde{f}_{kj}}$ , with *difference Fresnel number*  $\tilde{f}_{kj}^{-1} \equiv \tilde{f}_k^{-1} - \tilde{f}_j^{-1}$ , introduced in [24]. In the following we will omit the explicit  $\xi$  dependence. We note that the summation in (13) has  $N(J) = \frac{J^2-J}{2}$  terms, *e. g.*  $N(2) = 1$  or  $N(3) = 3$ . Especially, for a single hologram,  $J = 1$ , no summand remains and  $\sigma_-(\tilde{M}) = 0$  for all  $\xi$ . Thus, phase retrieval from a single hologram without homogeneity assumption is unstable for all frequencies, without additional regularity assumptions.

As we mention above, vanishing singular values correspond to unstable phase retrieval for those frequencies. Thus, we approximate  $\sigma_-(\tilde{M})$  from below by  $\sigma_{-,lb}(\tilde{M})$ ,

$$\sigma_-^2(\tilde{M}) \geq \sigma_{-,lb}^2(\tilde{M}) \equiv \frac{1}{J} \sum_{k=1}^J \sum_{j=k+1}^J \sin^2 \chi_{kj}, \quad (14)$$

which shows good agreement for low contrast transfer  $\sigma_-^2(\tilde{M}) \ll 1$ , see Figure 1.

More importantly, this allows us to make a direct comparison to the singular value of the homogeneous CTF matrix  $\tilde{M}_\gamma$ , given by,

$$\sigma^2(\tilde{M}_\gamma) = \sum_j (\sin \chi_j + \gamma \cos \chi_j)^2, \quad (15)$$

with phase chirp  $\chi_j \equiv \frac{|\xi|^2}{4\pi\tilde{f}_j}$ .

By comparing (15) with (14) it is evident that the lower stability bounds of the inhomogeneous CTF has a similar structure as a pure phase CTF, *i. e.*  $\sigma^2(\tilde{M}_0) = \sum_j \sin^2 \chi_j$ , but with dependence on the *difference* Fresnel number.

In fact, for a reconstruction of two holograms at different Fresnel numbers, the stability of the inhomogeneous CTF can be seen as proportional to a *single hologram* pure phase CTF reconstruction, but at effective difference Fresnel number [24]. Therefrom, we argue that inhomogeneous CTF reconstructions *without additional constraints* need at least two holograms at different Fresnel numbers. To stabilize the reconstruction, three or more holograms at different Fresnel numbers are favorable.

The Fresnel holographic phase retrieval is known to be sensitive to noise in the lower frequencies, especially in case of a pure phase object [22, 31], which relates to the vanishing singular value for  $\xi \rightarrow 0$ . In case of a homogeneous, non-pure phase object, *i. e.*  $\gamma > 0$ , this is circumvented by the contribution of the non-zero cosine term, see Fig. 1 especially the left sub-figure. Thus, the homogeneity assumption has an important stabilizing effect.

In Fig. 1 we illustrate our above analysis by an plot of the (squared) singular values for an exemplary set of Fresnel numbers of  $\tilde{f}_j$ , which are  $2.50 \times 10^{-3}$ ,  $2.45 \times 10^{-3}$ ,  $2.40 \times 10^{-3}$  and  $2.39 \times 10^{-3}$ , and set  $\gamma = 0.01$ . The corresponding six difference Fresnel numbers  $\tilde{f}_{kj}$  are  $4.41 \times 10^{-1}$ ,  $1.23 \times 10^{-1}$ ,  $1.18 \times 10^{-1}$ ,  $9.28 \times 10^{-2}$ ,  $6.00 \times 10^{-2}$  and  $5.28 \times 10^{-2}$ . In Fig. 1 we see, that the inhomogeneous CTF (smallest) singular value  $\sigma_-^2(\tilde{M})$  is a lower envelope of the pure phase CTF singular value  $\sigma_-^2(\tilde{M}_0)$ .

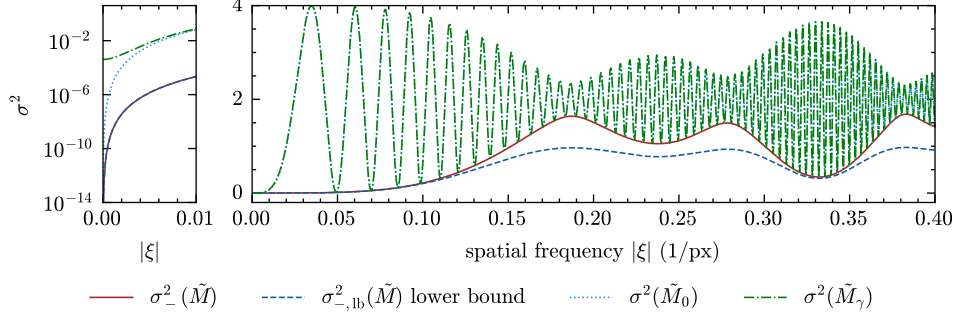


Fig. 1. Squared smallest singular values  $\sigma$  of CTF Fourier transfer matrices  $\tilde{M}$  without homogeneity assumption respectively  $\tilde{M}_\gamma$  ( $\gamma = 0.01$ ) with homogeneity for a set of four Fresnel numbers  $\tilde{f}_j$   $2.50 \times 10^{-3}$ ,  $2.45 \times 10^{-3}$ ,  $2.40 \times 10^{-3}$  and  $2.39 \times 10^{-3}$ . **Left** subfigure shows zoom into lower frequencies behavior, **right** larger frequency range. We can observe that  $\sigma^2(\tilde{M})$  is a lower envelope for  $\sigma^2(\tilde{M}_0)$ . Note that the oscillations for  $\sigma^2(\tilde{M})$  depend on the *difference* Fresnel numbers instead of the Fresnel number, as  $\sigma(\tilde{M}_\gamma)$ ,  $\sigma(\tilde{M}_0)$  do. An approximation from below for  $\sigma^2(\tilde{M})$  is shown by  $\sigma^2_{-,lb}(\tilde{M})$  defined in (14), with good agreement if  $\sigma^2 \ll 1$ .

### 3.1. Regularization strategy

Based on our observation that the stability of the inhomogeneous CTF relates to the pure phase CTF's stability at effective difference Fresnel numbers, we conclude that a similar regularization strategy as usually employed for the homogeneous CTF should be suitable. *I. e.* a frequency-dependent (or frequency weighting) regularization value  $\alpha(\xi)$  that separates the manifested singularity around  $\xi \approx 0$  and higher frequencies regime with transition at the first pure-phase CTF maxima [15, 16].

To account for the different orders of magnitudes of phase and absorption contrast for weak samples (for  $\sim 10$  keV and light elements or compounds, we have  $\delta \sim 10^{-6}$  and  $\beta \sim 10^{-9}$ ), we employ regularization in phase and absorption individually. Hence, the Tikhonov-type frequency regularization operator  $A$  becomes a diagonal operator given by  $A(\xi) = \text{diag}\left(2\sqrt{\alpha_\phi(\xi)}, 2\sqrt{\alpha_\mu(\xi)}\right)$ .

## 4. Experimental evaluation

### 4.1. Experimental data

We evaluate the performance of CTF-based phase retrieval with experimental data taken on the so-called *Göttinger Instrument for Nano-Imaging with X-rays* (GINIX) [3] located at the beamline P10 of the PETRA III storage ring at DESY, Hamburg, Germany. We used the waveguide focussed high-resolution nano-imaging setup in magnifying divergent beam geometry. The X-ray waveguide acts as quasi-point source for a clean illumination wavefront. For the experiment the X-ray energy was set to 13.8 keV. The diffraction patterns were recorded with the scintillator-based Andor Zyla 5.5 sCMOS camera, with a pixel size of 6.5  $\mu\text{m}$ .

By transaxial translation of the sample along the optical axis different propagation distances between sample and detector, thus Fresnel numbers, are recorded. By the Fresnel scaling theorem (see *e. g.* [7, 32]) the near-field diffraction patterns taken in the divergent beam geometry (spherical wavefronts) can be transformed into an equivalent effective parallel beam coordinate system (plane wavefronts). In line with our results from section 3, we acquired holograms at four defocussed distances corresponding to effective (parallel beam) Fresnel numbers  $\tilde{f}_j$   $1.84 \times 10^{-3}$ ,  $1.81 \times 10^{-3}$ ,  $1.78 \times 10^{-3}$  and  $1.73 \times 10^{-3}$ . To increase the signal-to-noise ratio, each hologram

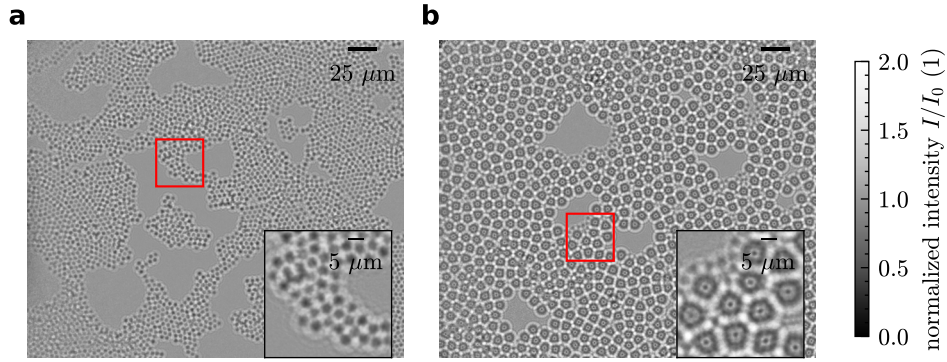


Fig. 2. Exemplary flat-field corrected holograms of colloidal sample used for phase retrieval. The effective Fresnel numbers is  $\bar{f} = 1.835 \times 10^{-3}$  at an effective pixel size 127.2 nm. Subfigure **a** shows mixture of 4.27  $\mu\text{m}$  silica and 4.24  $\mu\text{m}$  polystyrene, **b** with 9.36  $\mu\text{m}$  silica and 4.24  $\mu\text{m}$  polystyrene. Insets corresponds to insets in reconstructions below.

is an average of 100 images. Intensity images are normalized by principal component analysis (PCA) synthesized empty images [33]. Examples of the holograms are shown in Figure 2.

To violate the homogeneous object assumption, we prepared samples with two materials, with different but known refractive properties. To this end, we mixed silica ( $\text{SiO}_2$ ) and polystyrene (PS) colloids. One sample with similar diameters of 4.27  $\mu\text{m}$  silica and 4.24  $\mu\text{m}$  polystyrene (see Fig. 2a), the other with 9.36  $\mu\text{m}$  silica and 4.24  $\mu\text{m}$  polystyrene (see Fig. 2b). To corresponding refractive properties at 13.8 keV are given in Table 1.

Compound	$\delta$	$\beta$	$\gamma = \frac{\beta}{\delta}$	density ( $\text{g}/\text{cm}^3$ )
Silica ( $\text{SiO}_2$ )	$1.86 \times 10^{-6}$	$1.60 \times 10^{-8}$	$8.61 \times 10^{-3}$	1.7
Polystyrene (PS)	$1.23 \times 10^{-6}$	$7.08 \times 10^{-10}$	$5.75 \times 10^{-4}$	1.1

Table 1. Real  $\delta$  (phase shift) and imaginary  $\beta$  (attenuation) parts of the complex refractive index for listed compounds at 13.8 keV X-ray energy. Source: [34].

#### 4.1.1. Silica and polystyrene colloids of equal size

We begin the experimental validation with the equally sized colloids mixture of silica and polystyrene. By this, the primary difference between the colloids is expected to be different ratios between absorption and phase shift index,  $\gamma = \beta/\delta$ .

We compared the four combinations of CTF phase retrieval, listed in 2.1.2. The retrieved phase images are shown in Figure 3. The reconstruction parameters are listed in Table 2. To compare the influence of the homogeneity assumption we need to compare top-to-bottom; comparison between unconstrained and negativity constrained reconstruction is left-to-right.

Overall, all phase reconstructions agree. If we look more closely, we observe oscillatory artifacts spreading across the image in the CTF reconstructions with homogeneity assumption (see Figure 3a-b). These oscillation can also be seen in the line profile given in subfigure Figure 3e. In direct comparison these are significantly reduced in the inhomogeneous CTF reconstruction. Albeit, these can also be observed at the edges of the inhomogeneous reconstructions. We attribute this to the 2D Gaussian-shaped illumination, which was focused centrally in the images.

$\alpha_\gamma(\text{low; high})$	0	$5 \times 10^{-3}$
$\gamma = \gamma(\text{SiO}_2)$	$8.61 \times 10^{-3}$	–
$\tau$	$1 \times 10^{-2}$	–
$\alpha_\phi(\text{low; high})$	$6 \times 10^{-5}$	$5 \times 10^{-3}$
$\alpha_\mu(\text{low; high})$	0	$5 \times 10^{-1}$
$\tau$	$1 \times 10^{-4}$	–

Table 2. Regularization and reconstruction parameters for homogeneous (first three rows) and inhomogeneous (last three rows) CTF. Two-level frequency regularization  $\alpha(\xi)$  is applied with cut-off frequency at the first pure phase CTF maxima. For the homogeneity regularization the  $\beta/\delta$ -ratio of the stronger absorbing material (here silica) is used, which produces less artifacts.  $\tau$  denotes to proximity parameter for the constrained CTF-ADMM, see (12).

Hence, closer to the edges of the detector the illumination was lower and in turn the noise ratio higher. Due to the lower stability of the inhomogeneous CTF, see section 3, this has a stronger influence on the reconstructions.

If we compare the negativity constrained reconstructions Figure 3**b,d** with the unconstrained ones Figure 3**a,c**, we see that wrong positive phase shifts (light gray areas) are corrected. Furthermore, low frequency background variations are suppressed. Furthermore, in the line profile Figure 3**e** we see that the unconstrained solutions (dashed lines) qualitatively follow the theoretical line, but the constrained solutions (solid lines) agree quantitatively.

#### 4.1.2. Silica and polystyrene with different diameter

For a second sample we replaced the equal sized silica colloids with silica colloids of  $9.36 \mu\text{m}$  diameter. Thus, the projected phase shifts for the silica colloids exceed  $\pi/4$  rad.

Generally, the result discussed in section 4.1.1 are also confirmed for this sample. In particular, here the oscillatory artifacts are pronounced for the homogeneous CTF and still significantly suppressed for the inhomogeneous CTF. However, deviation from the expected phase shift can be observed in both reconstructions. Most notably, the central “dot” within the colloids is a persistent artifact in both reconstructions (and not a feature of the colloids).

## 5. Discussion & Outlook

To summarize, we have compared CTF-based phase retrieval, with the homogeneous object assumption (*homogeneous CTF*), introduced in subsection 2.1.1, and without it (*inhomogeneous CTF*). In combination with frequency-dependent regularization individually in phase and absorption by an diagonal regularization operator  $A = \text{diag}(2\sqrt{\alpha_\phi}, 2\sqrt{\alpha_\mu})$  and objects constraints, for example (non-)negativity, imposed on the reconstruction, we showed that inhomogeneous CTF inversion is possible, and even more so shows less oscillatory artifacts compared to the homogeneous CTF.

For both datasets tested, the inhomogeneous CTF showed superior image quality and more faithful results compared to the homogeneous CTF, especially when combined with negativity object constraint. In contrast, if the same dataset is reconstructed with the homogeneous CTF, we observe oscillatory artifacts, see Figure 3**a,c** and Figure 4**a**. Thus, we interpret the homogeneous CTF to be overly restrictive or inexact for non-homogeneous samples. As a result, such reconstructions are imprinted with artifacts.

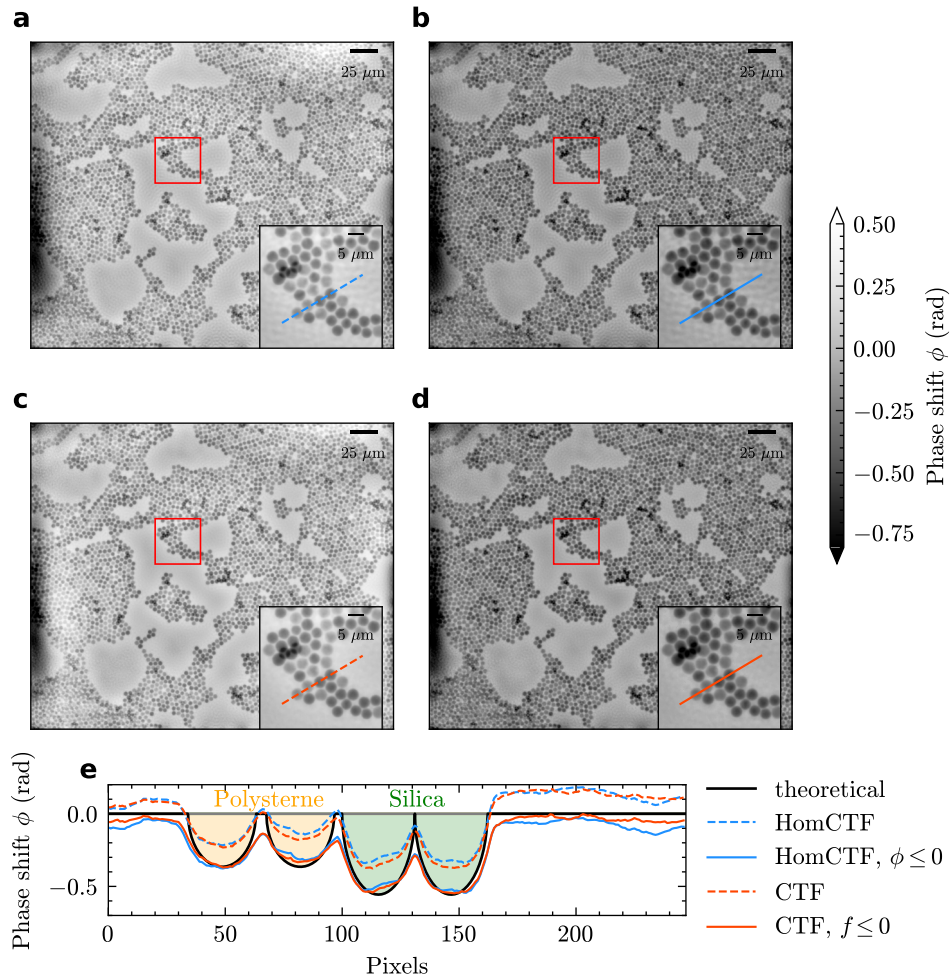


Fig. 3. CTF phase reconstructions of 4.27  $\mu\text{m}$  silica and 4.24  $\mu\text{m}$  polystyrene colloids sample. Top row **a**, **b** shows standard CTF-based phase retrieval with homogeneous object assumption, denoted as *HomCTF*. Bottom row **c**, **d** show our proposed approach without homogeneous object assumption. Left column **a**, **c** reconstructions are single-step without object constraints; right column are reconstruction with negativity constraint ( $f \leq 0$ ) computed with ADMM. Overall, all reconstructions agree. This shows, faithful CTF reconstructions are possible also without the homogeneity assumption. Moreover, CTF inversion without homogeneity constraint show less background oscillations; compare top row to bottom row. Hence, the background with homogeneity constraint is more uniform. Subfigure **e** shows a line profile indicated in the inset zoom plots of the reconstructions is shown over a theoretical expectation of the phase shifts. Pixel size is 127.2 nm.

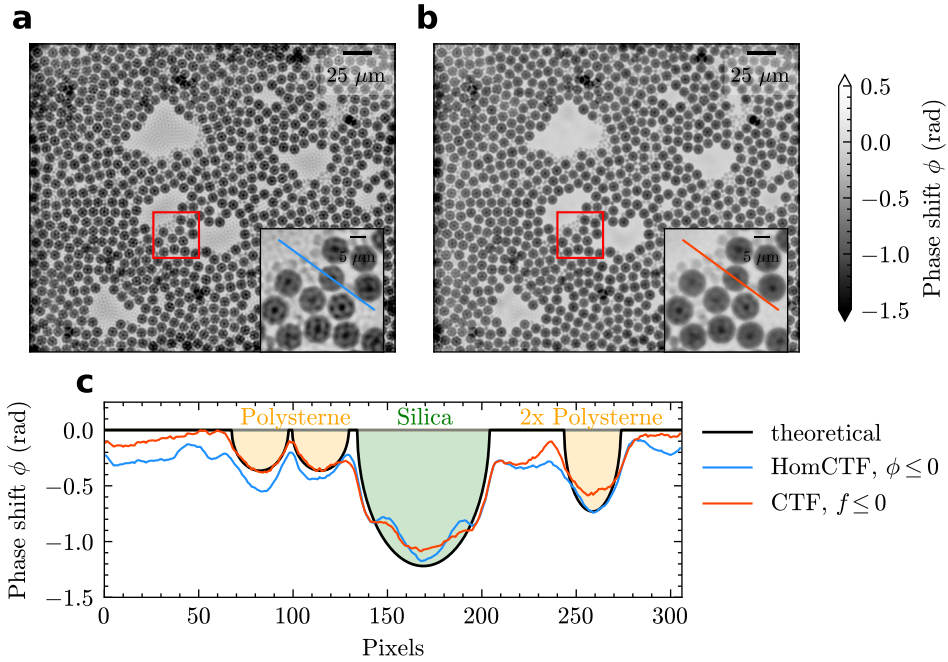


Fig. 4. CTF phase reconstructions of  $9.36\ \mu\text{m}$  silica and  $4.24\ \mu\text{m}$  polystyrene colloids sample. Subfigure **a** shows reconstruction with homogeneity assumption (HomCTF) and **b** without. Both reconstructions are with negativity constraint, *i. e.*  $\phi$  respectively  $f \leq 0$ . Corresponding line scans as indicated in the phase images are shown in **c**. The reconstruction with homogeneity shows prominent oscillatory artifacts, which are present in the background as well as in the colloids, whereas the CTF without homogeneity overall is closer to the theoretical curve, albeit deviations can be observed. The central dots within the larger colloids are artifacts appearing in both reconstructions. Pixel size is  $127.2\ \text{nm}$ .

For the colloids with  $4\ \mu\text{m}$  diameter, as discussed in subsection 4.1.1, the theoretical expected phase shifts are  $\phi \leq \pi/4$  rad. In comparison to the sample of subsection 4.1.2 with larger colloids, the expected phase shifts partly exceed  $\pi/4$  rad. For the latter, more pronounced oscillatory artifacts can be observed when reconstructed with homogeneity assumption. Again, the inhomogeneous CTF is less imprinted with those artifacts, albeit for the second sample deviations for larger phase shifts ( $\geq 0.5$  rad) can be seen. Thus, we relate these artifacts in the homogeneous CTF to be partly caused by nonlinearity errors, which in turn can be better compensated in the less restricted inhomogeneous CTF, allowing qualitatively superior results.

We note that the CTF inversion as linear inverse problem allows computationally fast reconstructions, also with constraints imposed via ADMM [15]. In the unconstrained case, it still is a one-step Fourier filter. The computational complexity from the homogeneous to inhomogeneous CTF is doubled, since the unknown variables are doubled from only  $\phi$  to  $f = (\phi, \mu)^\top$ . Still, it has a considerably less computational burden as any nonlinear method. This can potentially be utilized for qualitative online reconstructions, directly on data acquisition.

Furthermore, we have analyzed the influence on the stability of the homogeneity assumption and found the stability of the inhomogeneous CTF to be the lower envelope of the stability of the pure phase CTF. We approximated the frequencies with near zero singular values, where inversion is sensitive to noise, of the inhomogeneous CTF by a structurally similar term as the

pure phase CTF singular value. We conclude that the stability of the inhomogeneous CTF can be related to be lower bounded by the pure phase CTF singular value, but at effective *difference Fresnel numbers*.

As a result, the well-known low-frequency instability of the (pure phase) CTF inversion also applies to the inhomogeneous CTF even more, but depending on the difference Fresnel number. Thus, optimal experimental settings are governed by the difference Fresnel number. Furthermore, we showed by example of four holograms recorded at different Fresnel numbers, that an inhomogeneous CTF reconstruction is feasible. The addition of prior knowledge via a constrained optimization using the ADMM algorithm yield results in good agreement with the theoretical predictions, see Fig. 3e respectively 4c.

Moreover, as we see for the larger colloids, in sec. 4.1.2, nonlinear effects start to interfere with linearized reconstruction methods. Also, stronger violations of the homogeneity assumption involve higher nonlinearity. Hence, naturally the question of the impact of the homogeneity constraint and its omission on nonlinear reconstruction raises. Albeit inhomogeneous nonlinear solvers exists, these usually need many iterations to converge.

A possible nonlinear extension to the CTF is a so-called *frozen Gauss-Newton* iteration [35]. Here, in contrast to a regular (iteratively regularized) Gauss-Newton method, the Fréchet derivative of the Fresnel imaging operator (1) is not (computationally expensive) computed in each iteration, but kept at the initial point  $f = 0$  (weak object limit). The derivative then coincides with the CTF operator [36]. This can be seen as addition of a nonlinearity term to the linear inverse problem of the CTF defined in (7).

Furthermore, in view of the stabilizing effect of the homogeneity constraint, as we discussed in section 3, a reasonable regularization strategy could be to regularize the deviation from the homogeneous solution instead in the basis of phase and absorption. Finally, depending on the object and experimental case, our work can also be used to justify the current use of the homogeneous CTF, based on dissecting the effects of (weak) non-homogeneity and non-linearity.

**Funding.** Deutsche Forschungsgemeinschaft (DFG) - Project number 432680300 (SFB 1456-C03).

**Disclosures.** The authors declare no conflicts of interest.

**Acknowledgments.** We thank Simon Huhn for the inspiring discussions and helpful comments.

**Data availability.** Data underlying the results presented in this paper are not publicly available at this time but may be obtained from the authors upon reasonable request.

## References

1. T. Salditt and M. Töpperwien, "Holographic imaging and tomography of biological cells and tissues," in *Topics in Applied Physics*, (Springer International Publishing, 2020), pp. 339–376.
2. P. J. Withers, C. Bouman, S. Carmignato, V. Cnudde, D. Grimaldi, C. K. Hagen, E. Maire, M. Manley, A. Du Plessis, and S. R. Stock, "X-ray computed tomography," *Nat. Rev. Methods Primers* **1** (2021).
3. T. Salditt, M. Osterhoff, M. Krenkel, R. N. Wilke, M. Priebe, M. Bartels, S. Kalbfleisch, and M. Sprung, "Compound focusing mirror and x-ray waveguide optics for coherent imaging and nano-diffraction," *J. Synchrotron Radiat.* **22**, 867–878 (2015).
4. C. Morawe, R. Barrett, P. Cloetens, B. Lantelme, J.-C. Peffen, and A. Vivo, "Graded multilayers for figured kirkpatrick-baez mirrors on the new esrf end station id16a," in *Advances in X-Ray/EUV Optics and Components X*, S. Goto, C. Morawe, and A. M. Khounsary, eds. (SPIE, 2015).
5. J. Soltau, M. Vassholz, M. Osterhoff, and T. Salditt, "In-line holography with hard x-rays at sub-15 nm resolution," *Optica* **8**, 818 (2021).
6. S. Maretzke and T. Hohage, *Constrained Reconstructions in X-ray Phase Contrast Imaging: Uniqueness, Stability and Algorithms* (Springer International Publishing, 2020), pp. 377–403.
7. D. Paganin, *Coherent X-Ray Optics*, vol. 6 of *Oxford Series on synchrotron radiation* (Oxford University Press, 2006).
8. D. Paganin, S. C. Mayo, T. E. Gureyev, P. R. Miller, and S. W. Wilkins, "Simultaneous phase and amplitude extraction from a single defocused image of a homogeneous object," *J. Microsc.* **206**, 33–40 (2002).
9. Y. D. Witte, M. Boone, J. Vlassenbroeck, M. Dierick, and L. V. Hoorebeke, "Bronnikov-aided correction for x-ray computed tomography," *J. Opt. Soc. Am. A* **26**, 890–894 (2009).
10. R. W. Gerchberg, "A practical algorithm for the determination of phase from image and diffraction plane pictures," *Optik* **35**, 237–246 (1972).

11. D. R. Luke, "Relaxed averaged alternating reflections for diffraction imaging," *Inverse Probl.* **21**, 37–50 (2004).
12. J. Hagemann, M. Töpperwien, and T. Salditt, "Phase retrieval for near-field x-ray imaging beyond linearisation or compact support," *Appl. Phys. Lett.* **113**, 041109 (2018).
13. V. Davidoiu, B. Sixou, M. Langer, and F. Peyrin, "Non-linear iterative phase retrieval based on frechet derivative," *Opt. Express* **19**, 22809 (2011).
14. F. Wittwer, J. Hagemann, D. Brückner, S. Flenner, and C. G. Schroer, "Phase retrieval framework for direct reconstruction of the projected refractive index applied to ptychography and holography," *Optica* **9**, 295 (2022).
15. S. Huhn, L. M. Lohse, J. Lucht, and T. Salditt, "Fast algorithms for nonlinear and constrained phase retrieval in near-field x-ray holography based on tikhonov regularization," *Opt. Express* **30**, 32871–32886 (2022).
16. P. Cloetens, W. Ludwig, J. Baruchel, D. Van Dyck, J. Van Landuyt, J. P. Guigay, and M. Schlenker, "Holotomography: Quantitative phase tomography with micrometer resolution using hard synchrotron radiation x rays," *Appl. Phys. Lett.* **75**, 2912–2914 (1999).
17. A. Kostenko, K. J. Batenburg, H. Suhonen, S. E. Offerman, and L. J. van Vliet, "Phase retrieval in in-line x-ray phase contrast imaging based on total variation minimization," *Opt. Express* **21**, 710–723 (2013).
18. P. Villanueva-Perez, F. Arcadu, P. Cloetens, and M. Stampanoni, "Contrast-transfer-function phase retrieval based on compressed sensing," *Opt. Lett.* **42**, 1133–1136 (2017).
19. K. Mom, M. Langer, and B. Sixou, "Nonlinear primal–dual algorithm for the phase and absorption retrieval from a single phase contrast image," *Opt. Lett.* **47**, 5389 (2022).
20. J. W. Goodman, *Introduction to Fourier optics* (Macmillan Learning, 2007), fourth edition ed.
21. L. D. Turner, B. B. Dhal, J. P. Hayes, A. P. Mancuso, K. A. Nugent, D. Paterson, R. E. Scholten, C. Q. Tran, and A. G. Peele, "X-ray phase imaging: Demonstration of extended conditions with homogeneous objects," *Opt. Express* **12**, 2960–2965 (2004).
22. S. Zabler, P. Cloetens, J.-P. Guigay, J. Baruchel, and M. Schlenker, "Optimization of phase contrast imaging using hard x rays," *Rev. Sci. Instruments* **76**, 073705 (2005).
23. S. Maretzke, "A uniqueness result for propagation-based phase contrast imaging from a single measurement," *Inverse Probl.* **31**, 065003, 16 (2015).
24. S. Maretzke and T. Hohage, "Stability estimates for linearized near-field phase retrieval in x-ray phase contrast imaging," *SIAM J. on Appl. Math.* **77**, 384–408 (2017).
25. P. Cloetens, W. Ludwig, J. Baruchel, J.-P. Guigay, P. Pernot-Rejmánková, M. Salomé-Pateyron, M. Schlenker, J.-Y. Buffière, E. Maire, and G. Peix, "Hard x-ray phase imaging using simple propagation of a coherent synchrotron radiation beam," *J. Phys. D: Appl. Phys.* **32**, A145–A151 (1999).
26. S. Boyd, N. Parikh, E. Chu, B. Peleato, J. Eckstein *et al.*, "Distributed optimization and statistical learning via the alternating direction method of multipliers," *Found. Trends Mach. learning* **3**, 1–122 (2011).
27. A. Beck, *First-Order Methods in Optimization*, MOS-SIAM Series on Optimization (Society for Industrial and Applied Mathematics, 2017).
28. H. H. Bauschke and P. L. Combettes, *Convex Analysis and Monotone Operator Theory in Hilbert Spaces* (Springer International Publishing, 2017).
29. P. L. Combettes and J.-C. Pesquet, *Proximal Splitting Methods in Signal Processing* (Springer New York, New York, NY, 2011), pp. 185–212.
30. T. Goldstein, B. O'Donoghue, S. Setzer, and R. Baraniuk, "Fast alternating direction optimization methods," *SIAM J. on Imaging Sci.* **7**, 1588–1623 (2014).
31. M. Langer, P. Cloetens, and F. Peyrin, "Regularization of phase retrieval with phase-attenuation duality prior for 3-d holotomography," *IEEE Trans. on Image Process.* **19**, 2428–2436 (2010).
32. T. Salditt, A. Egner, and D. R. Luke, eds., *Nanoscale Photonic Imaging* (Springer International Publishing, 2020).
33. J. Hagemann, M. Vassholz, H. Hoeppe, M. Osterhoff, J. M. Rosselló, R. Mettin, F. Seiboth, A. Schropp, J. Möller, J. Hallmann, C. Kim, M. Scholz, U. Boesenberg, R. Schaffer, A. Zozulya, W. Lu, R. Shayduk, A. Madsen, C. G. Schroer, and T. Salditt, "Single-pulse phase-contrast imaging at free-electron lasers in the hard x-ray regime," *J. Synchrotron Radiat.* **28**, 52–63 (2021).
34. T. Schoonjans, A. Brunetti, B. Golosio, M. S. del Rio, V. A. Solé, C. Ferrero, and L. Vincze, "The xraylib library for x-ray–matter interactions. recent developments," *Spectrochimica Acta Part B: At. Spectrosc.* **66**, 776–784 (2011).
35. Q. Jin, "On a class of frozen regularized gauss-newton methods for nonlinear inverse problems," *Math. Comput.* **79**, 2191–2211 (2010).
36. S. Maretzke, M. Bartels, M. Krenkel, T. Salditt, and T. Hohage, "Regularized newton methods for x-ray phase contrast and general imaging problems," *Opt. Express* **24**, 6490–6506 (2016).

### A. Determinant of the transfer matrix

The determinant  $D$  used in (9) with regularization  $A = \text{diag}(2\sqrt{\alpha_\phi}, 2\sqrt{\alpha_\mu})$  is given by

$$\begin{aligned}
 D &\equiv \det(M^*M + A^*A) \\
 &= \det \left\{ \begin{pmatrix} 4 \sum_j s_j & 4 \sum_j s_j c_i \\ 4 \sum_j s_j c_i & 4 \sum_j s_j \end{pmatrix} + \begin{pmatrix} 4\alpha_\phi & 0 \\ 0 & 4\alpha_\mu \end{pmatrix} \right\} \\
 &= \left( 4\alpha_\phi + 4 \sum_j s_j^2 \right) \left( 4\alpha_\mu + 4 \sum_j c_j^2 \right) - \left( 4 \sum_j c_j s_j \right)^2 \\
 &= 16 \left\{ \alpha_\mu \alpha_\phi + \alpha_\mu \sum_j s_j^2 + \alpha_\phi \sum_j c_j^2 + \left( \sum_j s_j^2 \right) \left( \sum_j c_j^2 \right) - \left( \sum_j c_j s_j \right)^2 \right\},
 \end{aligned} \tag{16}$$

where sums are meant as summation from  $j = 1$  to  $j = J$ .